Cassini observations of Saturn's inner plasmasphere: Saturn orbit insertion results

E.C. Sittler Jr.[a,*], M. Thomsen[b], R.E. Johnson[c], R.E. Hartle[a], M. Burger[a], D. Chornay[a], M.D. Shappirio[a], D. Simpson[a], H.T. Smith[c], A.J. Coates[d], A.M. Rymer[e], D.J. McComas[f], D.T. Young[f], D. Reisenfeld[g], M. Dougherty[h], N. Andre[d,i]

[a]NASA Goddard Space Flight Center, Code 612.2, 8800 Greenbelt Road, Greenbelt, MD 20771, USA
[b]Los Alamos National Laboratory, NM, USA
[c]University of Virginia, Charlottesville, VA, USA
[d]Mullard Space Science Laboratory, UK
[e]Johns Hopkins Applied Physics Laboratory, MD, USA
[f]Southwest Research Institute, San Antonio, TX, USA
[g]University of Montana, MT, USA
[h]Imperial College, London, UK
[i]Research and Scientific Support Department, European Space Agency, The Netherlands

Abstract

We present new and definitive results of Cassini plasma spectrometer (CAPS) data acquired during passage through Saturn's inner plasmasphere by the Cassini spacecraft during the approach phase of the Saturn orbit insertion period. This analysis extends the original analysis of Sittler et al. [2005. Preliminary results on Saturn's inner plasmasphere as observed by Cassini: comparison with Voyager. Geophys. Res. Lett. 32, L14S07, doi:10.1029/2005GL022653] to $L \sim 10$ along with also providing a more comprehensive study of the interrelationship of the various fluid parameters. Coincidence data are sub-divided into protons and water group ions. Our revised analysis uses an improved convergence algorithm which provides a more definitive and independent estimate of the spacecraft potential Φ_{SC} for which we enforce the protons and water group ions to co-move with each other. This has allowed us to include spacecraft charging corrections to our fluid parameter estimations and allow accurate estimations of fluctuations in the fluid parameters for future correlative studies. In the appendix we describe the ion moments algorithm, and minor corrections introduced by not weighting the moments with $\sin\theta$ term in Sittler et al. [2005] (Correction offset by revisions to instruments geometric factor). Estimates of the spacecraft potential and revised proton densities are presented. Our total ion densities are in close agreement with the electron densities reported by Moncuquet et al. [2005. Quasi-thermal noise spectroscopy in the inner magnetosphere of Saturn with Cassini/RPWS: electron temperatures and density. Geophys. Res. Lett. 32, L20S02, doi:10.1029/2005GL022508] who used upper hybrid resonance (UHR) emission lines observed by the radio and plasma wave science (RPWS) instrument. We show a positive correlation between proton temperature and water group ion temperature. The proton and thermal electron temperatures track each with both having a positive radial gradient. These results are consistent with pickup ion energization via Saturn's rotational electric field. We see evidence for an anti-correlation between radial flow velocity V_R and azimuthal velocity V_ϕ, which is consistent with the magnetosphere tending to conserve angular momentum. Evidence for MHD waves is also present. We show clear evidence for outward transport of the plasma via flux tube interchange motions with the radial velocity of the flow showing positive radial gradient with $V_R \sim 0.12(L/4)^{5.5}$ km/s functional dependence for $4 < L < 10$ (i.e., if we assume to be diffusive transport then $D_{LL} \sim D_0 L^{11}$ for fixed stochastic time step δt). Previous models with centrifugal transport have used $D_{LL} \sim D_0 L^3$ dependence. The radial transport seems to begin at Enceladus' L shell, $L \sim 4$, where we also see a minimum in the W^+ ion temperature $T_W \sim 35$ eV. For the first time, we are measuring the actual flux tube interchange motions in the magnetosphere and how it varies with radial distance. These observations can be used as a constraint with regard to future

---

*Corresponding author. Tel.: +1 301 2869215.
E-mail address: edward.c.sittler@nasa.gov (E.C. Sittler Jr.).

transport models for Saturn's magnetosphere. Finally, we evaluate the thermodynamic properties of the plasma, which are all consistent with the pickup process being the dominant energy source for the plasma.

1. Introduction

The relationship between Voyager plasma measurements and Cassini results were presented in Sittler et al. (2005) using coincidence ion data by the Cassini plasma spectrometer (CAPS) instrument during the approach phase of the SOI period. This comparison was based on preliminary results. Evidently, Cassini entered the magnetosphere during a quiescent period similar to that for the Voyager encounters (see Bridge et al., 1981, 1982; Lazarus and McNutt, 1983; Sittler et al., 1983; Richardson, 1986; Richardson and Sittler, 1990). Pioneer 11 spacecraft probed Saturn's magnetosphere in 1979 when the magnetosphere was highly compressed during passage of a compression region in the solar wind (Wolfe et al., 1980; Frank et al., 1980).

Our results are more definitive than that be Sittler et al. (2005), since we are using an improved convergence algorithm for our ion moment determinations while also enforcing the protons and water group ions to co-move. This latter feature allows for an independent determination of the spacecraft potential. Our analysis is confined to distances beyond $L \sim 3$, since the instruments high voltage was lowered for the SOI insertion burn for instrument health and safety reasons. In Fig. 1, we show the trajectory for SOI. During SOI the spacecraft approached and exited Saturn's magnetosphere at mid-latitudes ($\lambda \sim -15°$), similar to that of Voyager 2 with ring plane crossings between the F and G rings ($L \sim 2.7$). As discussed in Sittler et al. (2005), the viewing was only optimal during the inbound pass and is reason outbound pass has not yet been analyzed.

2. Instrument description and ion composition

The CAPS instrument (Young et al., 2004) is composed of three separate particle instruments: ion mass spectrometer (IMS), electron spectrometer (ELS) and an ion beam spectrometer (IBS). The IMS, using time-of-flight (TOF) technology, has a composition capability. It makes 62 contiguous ion measurements in E/Q between 1 v and 50 kV with energy resolution of 17%. The IMS has an intermediate mass resolution capability, called straight through (ST) and a high mass resolution capability that produces linear electric field (LEF) data (McComas et al., 1990, 1998; McComas and Nordholt, 1990). The LEF technique, which is isochronous in TOF for atomic species, has the ability to separate molecular species of the same M/Q by detuning the upper section of the LEF section (Nordholt et al., 1998). To better understand instrument

word usage we refer to the *Space Science Review* article by Young et al. (2004). During data acquisition the IMS electronics accumulates the coincidence ion counts within predetermined TOF buckets for protons, for each of the water group ions, and for other minor species. There were miss-alignment of TOF buckets and their resolution is discussed in Sittler et al. (2005). Coincidence ion counts are measured over the full energy range and 8 angular sectors of the IMS. The 8 angular sectors, confined to what we call the collimator plane, cover a field-of-view (FOV) of 160° with a resolution of $8° \times 20°$ (Young et al., 2004). The
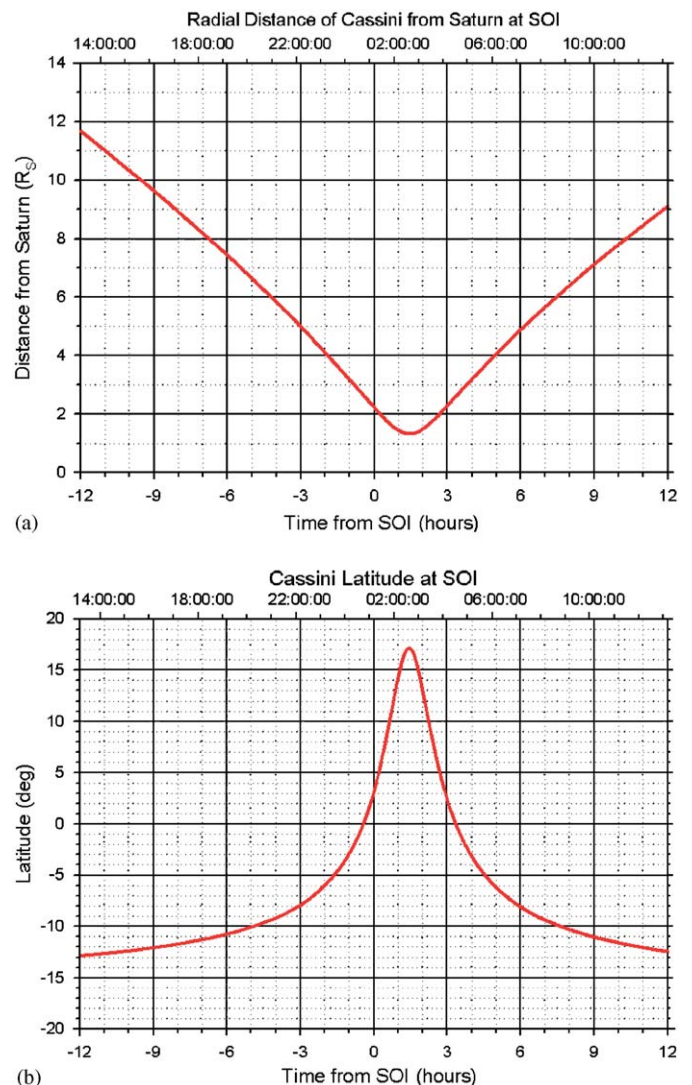

Fig. 1. Plot (a) shows the radial distance of the Cassini spacecraft with respect to Saturn's center as a function of spacecraft event time (SCET) for the SOI trajectory. In plot (b), we correspondingly show the spacecraft latitude relative to Saturn's equatorial plane.

FOV is aligned parallel to the spacecraft Z-axis and can be actuated over a range of $\sim 180°$ perpendicular to the spacecraft Z-axis (i.e., collimator plane is tilted in wind-shield wiper mode around spacecraft Z-axis). However, during this particular period, the actuator was in a fixed position, so that our measurements are essentially 2D in velocity space. The data were analyzed at a time resolution ~ 32 s for ions (a time resolution of 16 s can be achieved with this data set) and ~ 2 s for electrons.

As reported in Young et al. (2005) and Sittler et al. (2005), the ion population within Saturn's inner magneto-sphere, is dominated by protons and water group ions (O^+, OH^+, H_2O^+, H_3O^+) with minor constituents of N^+ ($\sim 5\%$) and O_2^+ (~ 1–2%). This composition of Saturn's inner magnetosphere has been also reported, for high-energy ions, by Krimigis et al. (2005). As in Sittler et al. (2005), we will only be presenting fluid parameters for H^+ and W^+, but eventually we expect to do the same for each sub-species of the water group ions (i.e., O^+, OH^+, H_2O^+, H_3O^+).

The ion composition spectrograms (Fig. 1 in Sittler et al., 2005) show the presence of self-induced background tails and background due to Saturn's radiation belts inside of Enceladus' orbit. Our fluid calculations for protons have approximately corrected for the leakage of the water group ion tails into the proton TOF channels at energies ~ 250 eV by comparing the amplitude of the proton signal relative to that for the main W^+ peaks in the TOF spectra and then subtracting this fraction from the measured proton counts. This can be seen in Fig. 2 which shows the leakage of water group ions into the proton TOF channels. For this particular example, the tails are $\sim 5\%$ of the main water group ion peak in their resident ion TOF channels. The leakage of protons into the W^+ TOF channels for energies < 100 eV is not important.

3. Fluid parameter results

3.1. Analysis

A quasi-moment technique was used to compute the fluid parameter by enforcing the ion flux for each species to be zero in the plasma frame of reference. The Appendix A discusses the algorithm in greater detail than in Sittler et al. (2005). We used a mean ion mass derived from the TOF data for the W^+ ions with $17 < M < 18$ with a time resolution ~ 15 min. Similarly, using the relative abundance of the water group ion species, we derived a mean geometric factor to estimate the phase space densities of the water group ions. Sittler et al. (2005) did not take into account the $\sin\theta$ dependence of velocity space volume element, $v^2\,dv\sin\theta\,d\theta\,d\phi$, sampled by the IMS (i.e., velocity space was over sampled). As shown in Appendix A, this results in an over-estimate of the density by $\sim \pi/2$. When we compare our $\sin\theta$ corrected total ion densities (i.e., used geometric factors from Sittler et al., 2005), $N_{\rm ION} = N_{\rm H} + N_{\rm W}$, with our ELS electron densities, $N_{\rm E}$, for the period 1600–1900 h, the ratio $N_{\rm E}/N_{\rm ION} \sim 1.5$, which is very close to the $\pi/2$ correction. This is a period of time when the presence of photo-electrons in the ELS measurements indicates that the spacecraft is positively charged. Under these conditions the ELS electron densities are considered reliable, and they can be corrected for spacecraft charging effects. We know that the time scale for isotropization of electrons via Coulomb collisions is $\tau_{e,iso} \sim 3$–4 min (Sittler et al., 2006a) in the vicinity of Dione. Since, resident time scales of the plasma is $\tau_{\rm R} \sim 5$ days at Dione (Richardson et al., 1998), we expect the thermal electrons to be isotropic or $\sqrt{T_\perp/T_\parallel} \sim 1$. The geometric factor for electrons is considered very reliable. Recent analysis of the ion geometric factors have uncovered an over estimate $\sim 50\%$ from that used by Sittler et al. (2005), which essentially offsets the $\sin\theta$ error (i.e., the instrument uses a deconvolution algorithm developed by Sittler (1993), which did not take into account events associated with "ghost peaks" which are caused by ion scattering within the instrument). The end result is ion densities that are essentially equivalent to that by Sittler et al. (2005).

4. Results

4.1. Overview

In Fig. 3, we show the results of our fluid calculations, for the period SCET182:1600–2400 h on 30 June 2004, as plots of ion number density N_i, ion flow velocity (i.e., $V_{\rm R}$, V_ϕ), and ion temperature T_i for both protons (red trace) and water group ions (blue trace). We also show the
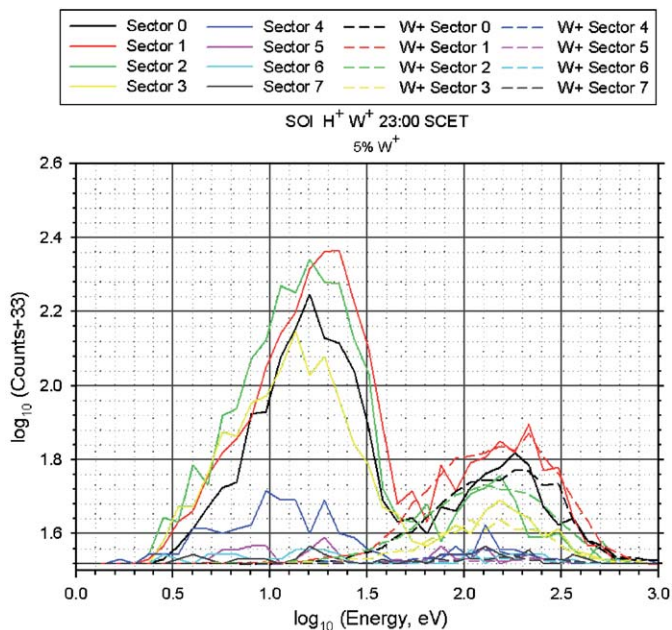

Fig. 2. Log–log plot of proton counts vs. proton energy (solid lines) and predicted water group ion counts (dashed lines), assuming 5% of observed water group ion counts, within proton TOF channels as a function of proton energy. Color is used to indicate angular sector.
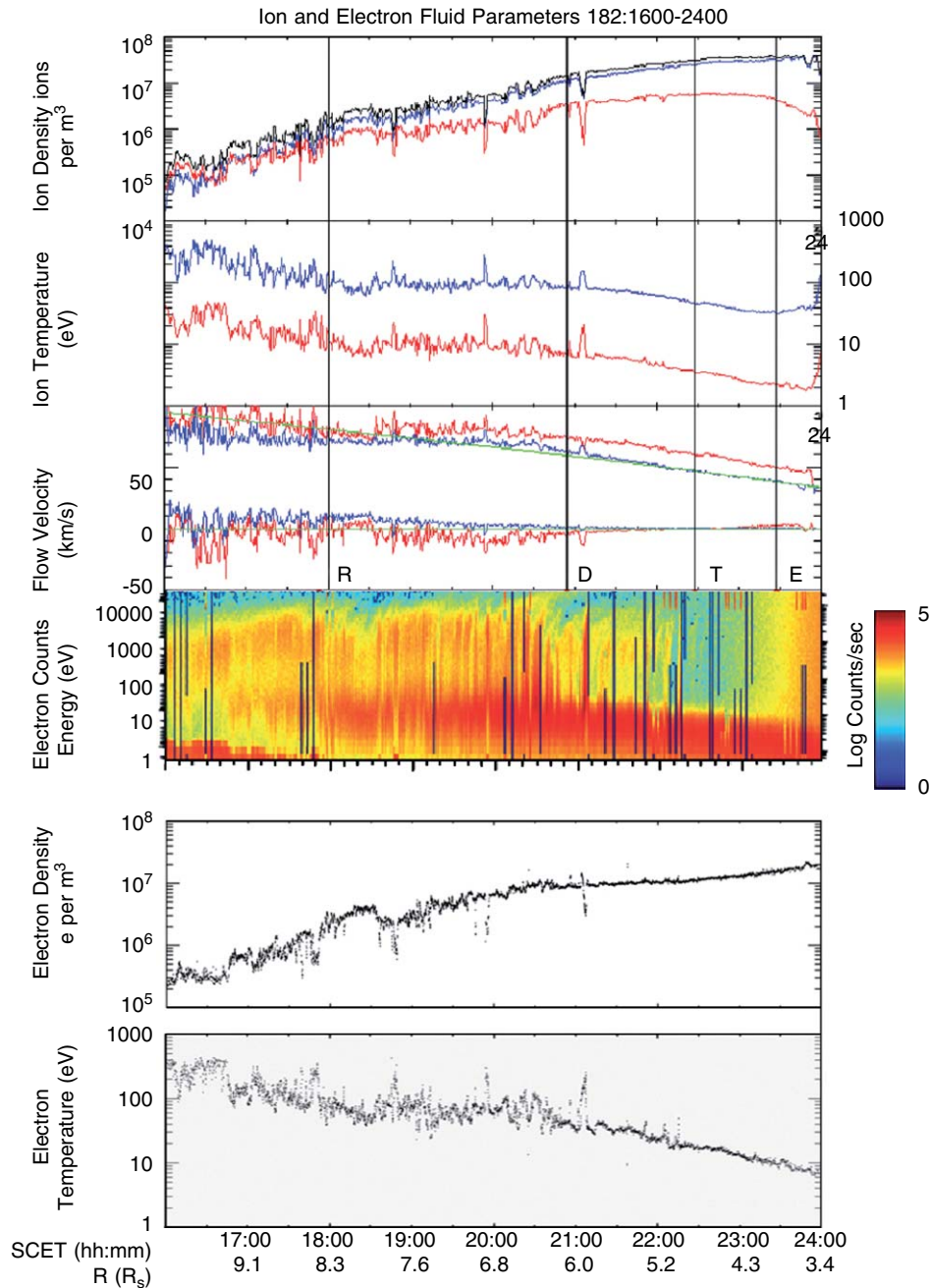
Fig. 3. In the upper three panels ion fluid parameters number density, temperature and flow velocity are displayed for protons (red) and water group ions (blue). Total ion density indicated in black. With regard to the flow velocity the corotation speed for azimuthal flow is indicated by the upper green line and the lower green line is for the cylindrical radial velocity to equal zero. The fourth panel shows energy–time color spectrogram for electron measurements, the fifth panel shows thermal electron number density and the lower panel shows the thermal electron temperature. The horizontal axis is the observation time in SCET for the period 182:1600–2400 h in 2004. The vertical lines labeled R, D, T and E indicate the times when the spacecraft crossed the dipole L shells of the moons Rhea, Dione, Tethys and Enceladus, respectively. Statistical errors are $\sim$5% at Rhea's L shell and decrease to $\sim$1% for W^+ and $\sim$2% for H^+ inside of Dione's L shell. Systematic errors $\sim +20\%$ are estimated for the density, $<8\%$ for the flow and $\sim +7\%$ for the temperature.

electron energy spectra in panel three from the bottom, electron density in second panel from bottom and thermal electron temperature in bottom panel. Here, we note that the electron density and temperature were derived from the Cassini-ELS using a Maxwellian fit to flux versus energy spectra below 100 eV, all data were taken from a central detector since these have been confirmed to be least affected by spacecraft affects and the data have been corrected by a positive spacecraft potential (Rymer, 2004). At around 1800 UT ($L \sim 8$) the spacecraft potential becomes negative as more electrons are flowing onto the spacecraft than are flowing off it, in this region the adopted method underestimates the local density. For the flow velocity data we use green traces to show $V_\phi = V_{COR}$ and

$V_R = 0$ for full corotation, respectively. We also show the total ion number density (black trace), which should be equal to the electron number density (i.e., $N_H + N_W = N_e$). Alignment is such that we only measure $T_\perp$ by assuming isotropy and overestimate N_H, N_W by the factor $\sqrt{T_\perp/T_\parallel}$. Therefore, we assume $T_\perp/T_\parallel \sim 2$ for H^+ and $T_\perp/T_\parallel \sim 5$ for W^+ based on Richardson and Sittler (1990) and Cassini RPWS results by Moncuquet et al. (2005) as discussed in Sittler et al. (2005). In the vicinity of Rhea, where trapped photoelectrons in the ELS energy spectra are present, the spacecraft potential $\Phi_{sc} > 0$ V, and the measured total ion density and electron density agree as expected.

Similar to that in Sittler et al. (2005), the data shows a large scale increase in the total ion density from $0.1\,\mathrm{cm}^{-3}$ at $L\sim10$, up to $40\,\mathrm{cm}^{-3}$ near Mimas' L shell. The proton densities reach a plateau and then decrease as the spacecraft nears the ring plane. This feature is consistent with centrifugal confinement of the heavy ion component, while the protons tend to float above the ring plane due to the ambipolar electric field (i.e., $T_H \sim T_{ec}$). Our total ion densities are very close to the electron densities by Moncuquet et al. (2005). The ion and electron temperatures show a large-scale decrease with decreasing r. In the case of water group ions we have $T_W \sim 100$–500 eV at $L\sim10$ to $T_W \sim 40$ eV at $L\sim3$. For protons we have $T_H \sim 10$–50 eV at $L\sim10$ to $T_H \sim 2$ eV at $L\sim3$. The thermal electrons behave similar to the protons with $T_{ec} < 1$ eV at $L \sim 3$. In the case of flow velocity, our results are consistent with corotation inside of Dione's L shell, while further out we see clear evidence of sub-corotation. We do see a minimum in the water group ion temperature near the L shell of Enceladus with $T_W \sim 35$ eV. This could be fortuitous, since the rise inside of Enceladus could be due to the presence of recently picked up ions near the equatorial plane, since the ambient ions have energies less than that for pickup ions (i.e., Sonic Mach number ~2). The apparent super-rotation of the protons is caused by a negative spacecraft potential as discussed in Sittler et al. (2005a) and quantitatively evaluated in the next section. Lastly, the thermal electron temperatures presented in Fig. 3 are very close to those estimated by Moncuquet et al. (2005). Their estimates are based on quasi-thermal noise (QTN) measured by the RPWS high frequency receiver. Their technique is different from ours and gives strong independent support for our results and visa versa.

4.2. Spacecraft charging calculations

In Appendix A we mention that we can iteratively shift the measurement points in energy by the spacecraft potential Φ_{SC} along a radial direction relative to the center of the spacecraft until the proton flow velocity is equal to the water group ion flow velocity. Here we assume the water group ions with energies ~250 eV are unaffected by spacecraft charging effects, where $\Phi_{SC} \sim 0$–10 v. The results of applying this algorithm are shown in Fig. 4, where one can see that the proton flow velocities track the W^+ ion flow velocities
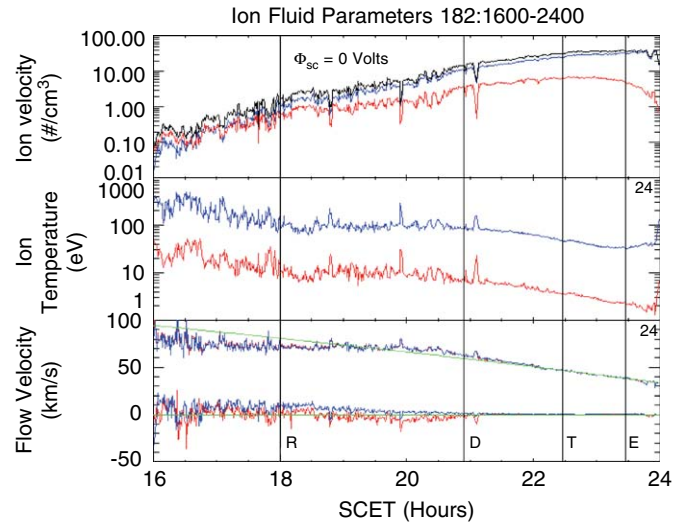

Fig. 4. Same as Fig. 3 upper three panels, except now we have adjusted the spacecraft potential, as described in the text, until the magnitude of the proton velocity equaled the water group ion flow velocity. As can be seen, the algorithm has worked quite well. As described in Figs. 5 and 6, only small changes in the proton density and proton temperature have resulted.
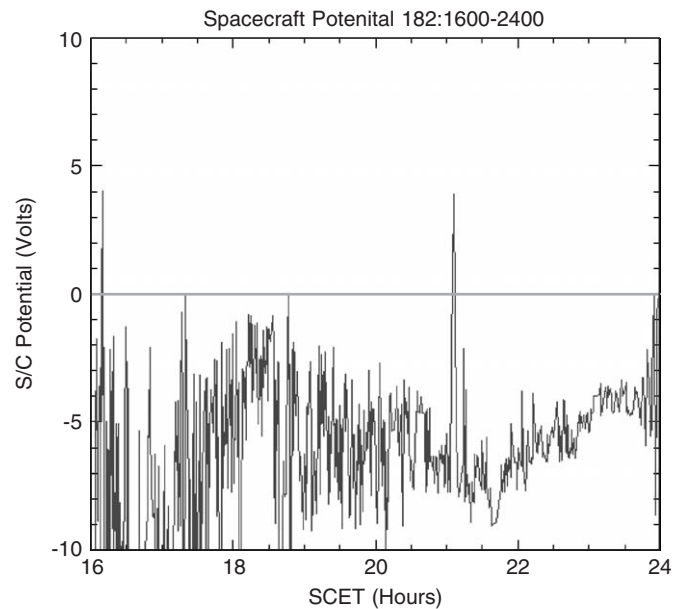

Fig. 5. Plot of the spacecraft potential Φ_{SC} as a function of SCET that was determined by enforcing the protons to co-move with the water group ions. Inside of Dione's L shell, the results are considered reliable, but outside, where the electron observations indicate a positive spacecraft potential via presence of photo-electrons, indicates some not yet understood systematic error is present in the proton velocity estimates.

very accurately and give the spacecraft potentials in Fig. 5. Differences in radial velocities introduce only a small correction to Φ_{SC}. Inside Dione's L shell, where we know the spacecraft is negatively charged, the potentials vary from $\Phi_{SC} \sim -7$ volts to $\Phi_{SC} \sim -3$ volts near Mimas' L shell. These are similar to the potentials predicted for E-ring grains (Jurac et al., 1995). Outside Dione's L shell, $\Phi_{SC} \sim -7$ volts

increases to $\Phi_{SC} \sim -2$ volts at Rhea's L shell, but then drops to large negative values $\Phi_{SC} < -10\,V$ outside Rhea's L shell where we know the spacecraft is positively charged from the ELS data. This indicates that for $L > 8.5$, the proton flow speeds have a systematic bias to higher flow speeds. This bias may be due to non-radial spacecraft potential electric fields which provide complex distortions of the proton velocity distributions at the instrument's entrance aperture. In Fig. 6, we use an independent estimate of the spacecraft potential; i.e., $\Phi_{SC} \sim (kT_{ec}/e) \ln(N_e/N_{ION})$, which is applicable for electrons. In the outer region, outside Rhea's L shell we get $\Phi_{SC} > 0\,V$ as expected, while inside of Rhea's L shell, where $N_{ION} > N_e$ we get negative spacecraft potentials $\Phi_{SC} \sim -3$ to $-1\,v$ similar to that derived in Fig. 5 by enforcing protons to co-move with water group ions. The similarity of the two curves after 1800 SCET, except for $\sim -3\,V$ offset of the co-moving solution relative to that in Fig. 6, gives credence to both techniques with systematic errors $\sim -3\,V$ and statistical errors $\sim \pm 2\,V$. We note that after 1800 h, photo-electrons are not present in the ELS observations, which indicates a negative spacecraft potential after 1800 SCET. So, the spacecraft potential may be offset by a few volts positive in Fig. 6 due to inter-calibration errors between ion-electron geometric factors $\sim 20\%$.

In Fig. 7, we show the ratio of the proton density for $\Phi_{SC} \neq 0$ and $\Phi_{SC} = 0$ as a function of time (i.e., proton densities in Figs. 3 and 4). There is a variable and slight increase in proton density by no more than 20% throughout the analysis interval 1600–2400 SCET. This

can be understood by equating the density to the ratio of the proton flux to the proton flow velocity, yielding a higher proton density for the same proton flux because the proton flow velocity is lower after correction for $\Phi_{SC} < 0$ volts. In Fig. 8 we have made a similar plot for proton temperature. Here, the proton temperature ratio varied with time less than $\pm 5\%$. This is expected, since the temperature is a higher order moment and protons of higher energies are more important for the velocity moment integrations. The higher-energy protons are less
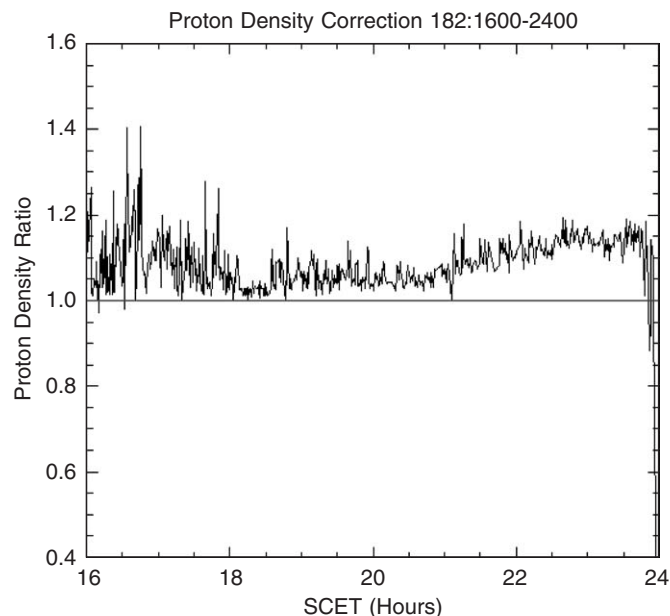

Fig. 7. Plot of the proton density ratio with $\Phi_{SC} \neq 0$ over that with $\Phi_{SC} = 0$, vs. SCET. Proton density estimates are revised upward by no more than $\sim 20\%$.
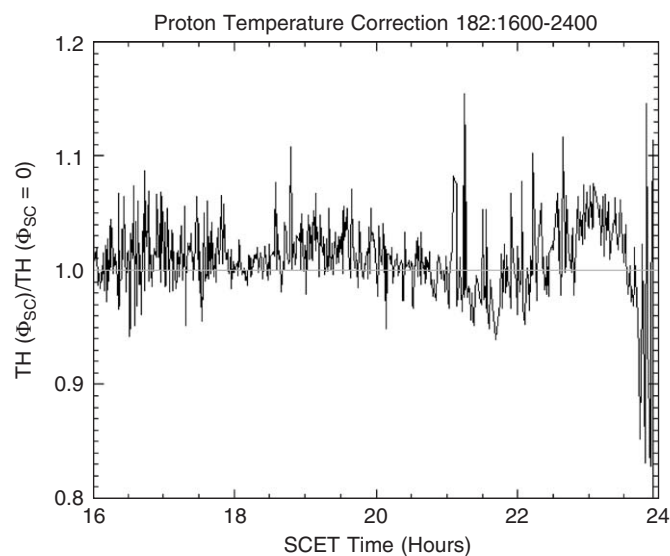

Fig. 8. Plot of the proton temperature ratio with $\Phi_{SC} \neq 0$ over that with $\Phi_{SC} = 0$, vs. SCET. As can seen the proton temperatures change by no more than $\pm 5\%$, due to the fact that the temperature is a higher order moment than density (i.e., at higher energies, proton's less sensitive to spacecraft charging effects).
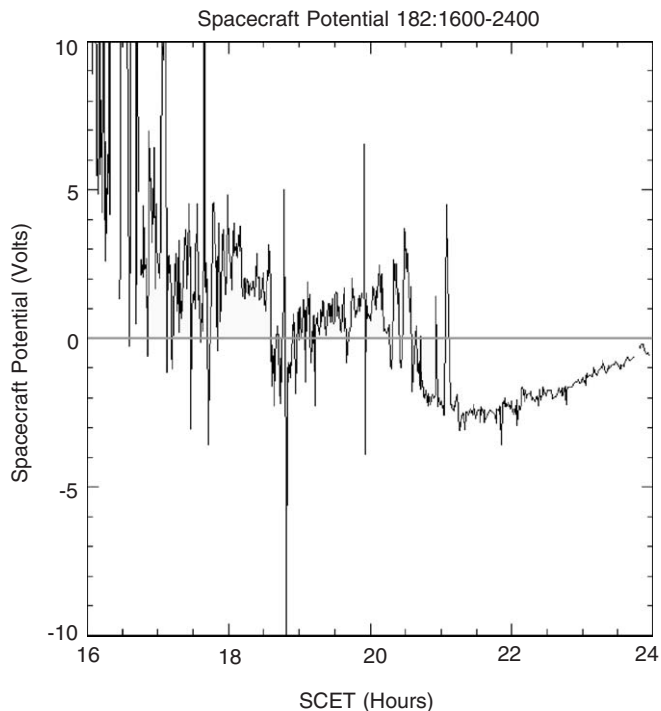

Fig. 6. Plot of the spacecraft potential Φ_{SC} determined from the relationship $\Phi_{SC} = (kT_{ec}/e) \ln(N_e/N_{ION})$. These results indicate a negative potential for times greater than 2000 SCET and are very similar to that in Fig. 5 based on H^+ and W^+ ions commoving.

affected by the spacecraft potential, so the corrections will be relatively lower.

5. Additional observational and theoretical considerations

In this section, we discuss observations of injection events as originally presented by Burch et al. (2005) and Hill et al. (2005) in the form of dispersion events, and Sittler et al. (2005) at the fluid level, along with transport issues. Injection events in Saturn's inner magnetosphere have been also analyzed by Mauk et al. (2005), and they have shown that effects of the large radial gradients in the global azimuthal rotational flow pattern often dominate the dispersive particle injection signatures. Both the injection events and flows are inter-related and will couple into ring current considerations discussed in Sittler et al. (2005), since static equilibrium must be violated to some degree if, for example, flux tube interchange motions are ongoing. We follow this section with evidence of anti-correlations between V_R and V_ϕ which can be caused by inter-change motions, injection events or compression-expansion of the magnetosphere (i.e., lower-frequency variations with periods $\sim 10\,\mathrm{s}$ of minutes to hours). These motions will result in the mixing of plasmas of different origins and eventually lead to the loss of plasma down the magnetotail as plasmoids (Cowley et al., 2005; Sittler et al., 2006b). We then present the first direct evidence of ongoing inter-change motions with an overall outward transport of the plasma. This is followed by an evaluation of the thermodynamic properties of the plasma that can be affected by transport (i.e., adiabatic cooling of outward moving flux tubes) or pickup process which can reveal itself in the form of "charge-exchange transport" as discussed by Johnson et al. (2005a). The pickup process energizes the plasma in the sense that its pickup energy will tend to increase with radial distance and provide a source of hot plasma in the outer magnetosphere. The latter effect and auroral consequences are discussed by Sittler et al. (2006b). Another related phenomena revealed by the data, is the correlation between the proton and thermal electron temperatures and which can be explained by the pickup process. The data is plotted in several formats to demonstrate the above issues.

5.1. Injection events and radial transport

Returning to Fig. 4, one can see deep density cavities where both protons and water group ions are hotter. The cavities have been identified by Burch et al. (2005) and Hill et al (2005) to be injection events coming from the outer magnetosphere. As a group, the cavities show evidence of negative radial velocities implying that they are injected radially inward (see Burch et al., 2005). Since the density and temperature anti-correlate, pressure balance will tend to be preserved at their boundaries. This anti-correlation will also tend to preserve total flux tube content, since hotter plasma of the same temperature anisotropy will have

a larger scale height and fill more of the flux tube toward higher latitudes (Sittler et al., 1983). The cavity just inside Dione's L shell, shows the proton azimuthal velocity decreasing toward the corotation velocity within the hot cavity. This can be understood by the fact that the protons are hotter and less sensitive to the spacecraft potential, and the lower density tends to make Φ_{SC} less negative. With $\Phi_{SC} \sim 0\,\mathrm{V}$ the protons are not accelerated across the spacecraft sheath and do not appear to be super-rotating. The water group ions will not be influenced by these effects and are thus the most reliable for measuring flow velocity.

The radial velocity of the water group ions also show a slight increase toward positive values with increasing radial distance. This is consistent with outward transport where the radial diffusion coefficient $D_{LL} \sim D_0 L^n$ and $n > 0$. To see this more clearly we have plotted in Fig. 9 the radial velocity of the water group ions on an expanded scale and since negative radial velocities can occur and since we are using a log scale, we have offset the velocities by $+1\,\mathrm{km/s}$. The apparent large negative spikes are just due to negative radial velocities. The data clearly shows an increase in outward radial transport with increasing radial distance. The observed variability with respect to the mean can be attributed to inter-change motions of both inward and outward moving flux tubes. The radial variation shows an $V_R \sim V_{R0}(L/L_0)^{5.5}$ (manual fit used with $V_{R0} \sim 0.12$ and $L_0 \sim 4.0$) variation which tends to saturate at $L \sim 12$ with values $< 40\,\mathrm{km/s}$. This must happen when one considers the radial velocities observed in the outer magnetosphere by Voyager (Sittler et al., 2006b). We estimate errors $< 2\%$ of the local corotation velocity for these measurements. So,
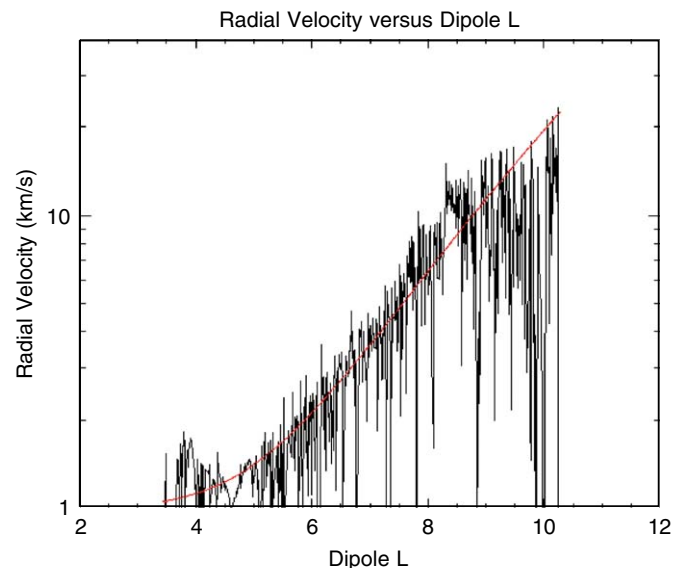

Fig. 9. A semi-log plot of cylindrical radial velocity of the flow for water group ions as a function of dipole L on a much-expanded scale than that shown in Fig. 4. The data has been offset by $+1\,\mathrm{km/s}$ since negative velocities can occur and a log scale is used. The red curve is a manual fit to the data with functional form $V_R = 1.0 + 0.12(L/4)^{5.5}$ (i.e., the $+1$ includes the offset).

some of the variability could be due to inaccuracies in the measurements (Note, that if this positive radial gradient was due to a systematic affect in the analysis, it would show a dependence proportional to L^n with $n\sim1$). If the transport is a stochastic process it will have the relationship $D_{LL}\sim V_R^2\delta t$ with δt a characteristic time scale for the inter-change motions (J.F. Cooper, private communication). If δt is independent of R, then $D_{LL}\sim D_0L^n$ with exponent of $n\sim11$ which is much higher than $n\sim3$ usually considered for centrifugally driven outward transport (see Richardson et al., 1998). The data does indicate, as noted above, a turn over in the variation of V_R with L so that $n\sim3$ may then be applicable within the outer magnetosphere. In a different parameterization for an effective diffusion "velocity" Schultz and Lanzerotti (1974) have $D_{LL}\sim V_RL$, so then we get $n\sim6.5$ and not $n\sim11$. With regard to centrifugally driven diffusion Siscoe and Summers (1981) get $n\sim6$ and that the diffusion coefficient is $\propto dNL^2/dL$, where NL^2 is the total flux tube content. Note, for purely diffusive transport, there would not be a systematic increase in V_R with L since mass flux occurs due to a density gradient in the mass density. But, we do expect δV_R to increase in amplitude with L which will enhance the radial diffusion coefficient D_{LL} with L as observed. Therefore, considering that both V_R and δV_R are increasing with L, we must be seeing a combination of diffusive and convective transport. The convective transport could be the result of non-linear terms in the centrifugal transport mechanism. In summary, these observations will impose a definite constraint on any future models of transport within Saturn's magnetosphere.

5.2. Velocity perturbations and conservation of angular momentum?

Inspection of Fig. 4 also shows that the radial velocity and azimuthal velocity are anti-correlated. This anti-correlation can also be seen in Fig. 10 where we have made a scatter plot of V_R/R vs. V_ϕ/R. The plot does show a lot of scatter which could be due to the presence of MHD waves super-imposed on the lower-frequency inter-change motions and/or expansion–contractions of the magneto-sphere. Further analysis may allow us to separate inter-change motions from MHD waves by comparing this data with magnetometer data (Andrè et al., 2006). Sittler et al. (2006b) developed an alternate model of Saturn's aurora to that of Cowley et al. (2005) and reported a similar effect in the Voyager plasma fluid parameters originally computed by Richardson (1986). This effect is consistent with the magnetosphere tending to conserve angular momentum. It will occur if the system torque is not sufficient to enforce corotation. This condition can be traced to the height integrated Pedersen conductivity in Saturn's ionosphere not being sufficiently large to support the required field aligned currents. These field-aligned currents oppose spinning up (i.e., $V_R<0$) or spinning down (i.e., $V_R>0$) of the magnetosphere.
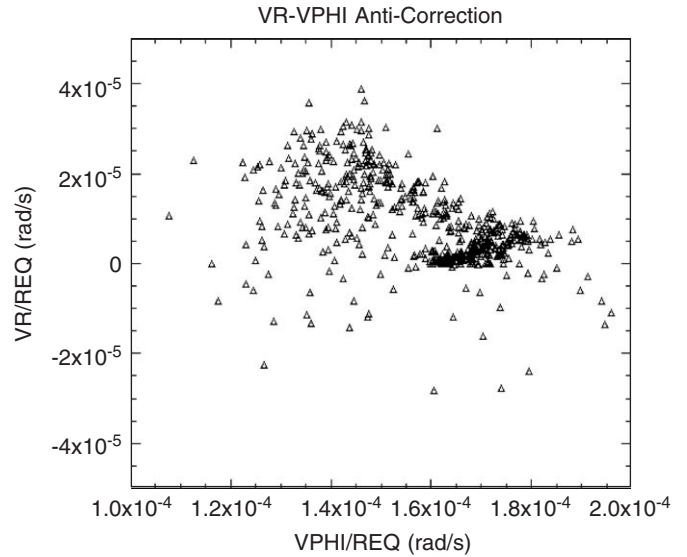

Fig. 10. Scatter plot of V_R/R vs. V_ϕ/R to show anti-correlation between V_R and V_ϕ. We have divided by equatorial radius R, since it is the angular velocity that is more appropriate with regard to the spin up and de-spin up of the magnetosphere.

5.3. Thermodynamic properties of the plasmasphere ions and electrons

In this section, we evaluate the thermodynamic properties of the plasma within Saturn's inner magnetosphere. To begin, we show a scatter plot of the proton temperature T_H vs. the water group ion temperature T_W in Fig. 11. As can be seen there is a positive correlation between T_H and T_W. In Figs. 3 and 4 and later in Fig. 15 the data shows a positive radial gradient in the ion temperatures. In Fig. 11 we have also super-imposed ratios of 6.7 (red), 10.0 (green) and 18.0 (blue). The red and blue lines bracket the data, while the green line gives the average trend for the total data set. If the protons were born initially as water group pickup ions, and then protons evolved over time in a manner similar to the water group ions, one might expect a ratio ~18 as indicated by the blue line. This will be true if the mean mass of the W^+ ions is ~18. This ratio tends to increase with decreasing radial distance, where O^+ being important for $L\sim10$ and H_3O^+ starts to dominate inside of $L\sim4$. On average the mean mass is ~17 a.m.u. for the period 1600–2400 h. For $T_H<10$ eV the data points move below the green line toward the blue line indicating their primary source is coming from pickup water group ions. As $T_H\sim2$ eV is approached the ratio can exceed 18 indicating heavier species such as H_3O^+ being the dominant pickup ion. Further out, where $T_H>10$ eV, the points have ratios less than 10 (i.e., reside above the green line) and could indicate that the protons are evolving in time differently than the water group ions. Either the protons are not cooling as fast, or some process is heating the protons relative to the water group ions. We note, when $T_W>100$ eV all the points reside above the blue line (i.e., ratios<18).
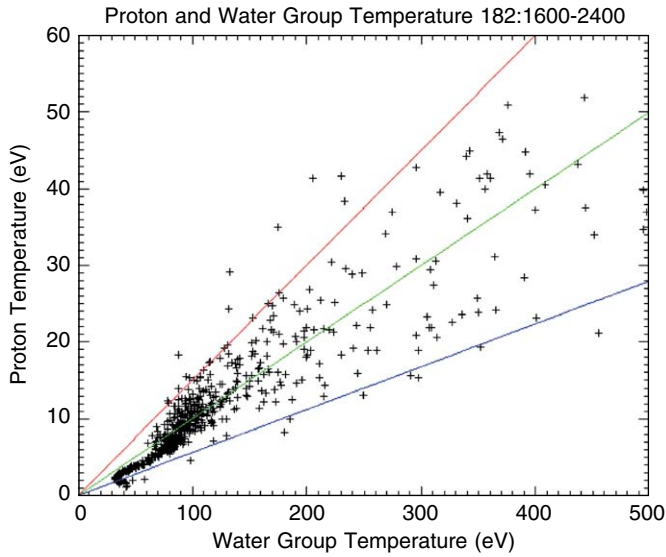
Fig. 11. Scatter plot of proton temperature vs. water group ion temperature. As can readily be seen, they are positively correlated, which is consistent with the pickup ion process to be the dominant energization mechanism for the ion population. The red, green and blue lines correspond to a T_{W+}/T_P ratio to be 6.7, 10.0 and 18.0, respectively.
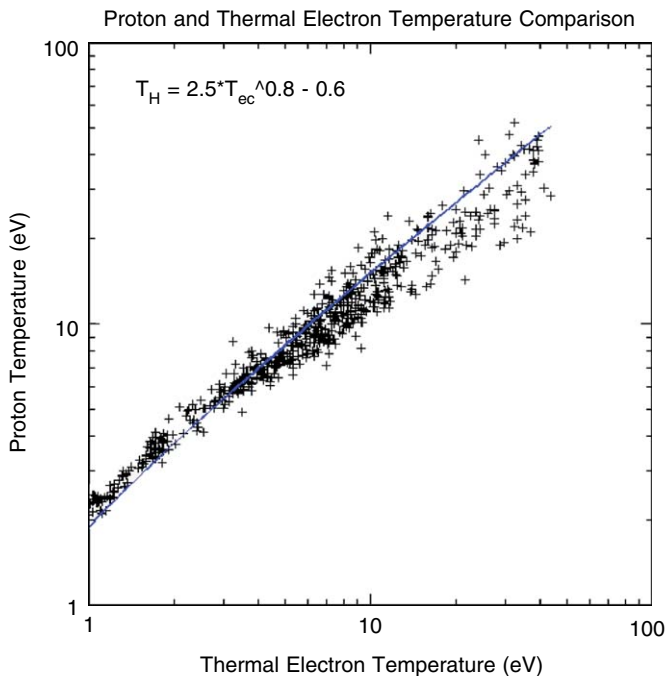

Fig. 12. Scatter plot of proton temperature vs. thermal electron temperature. There is a clear one to one correlation between the two temperatures with a manually derived power law fit super-imposed.

In Fig. 12, we show a scatter plot of the proton temperature T_H vs. the thermal electron temperature T_{ec}. The plot shows an almost one to one positive correlation between the two data sets. This suggests a mechanism for heating protons and electrons similar to the one first suggested by Barbosa (1986) for Jupiter and Barbosa (1987) for Saturn. That is when the ions are picked up a

two-stream instability results which accelerates the electrons (i.e., hot component) along the magnetic field via lower hybrid waves when their energies are proportional to the ion pickup energy. Then Coulomb collisions, especially inside of Rhea's orbit, will tend to isotropize the hot electrons and heat the thermal electron population. This result is not unexpected. It would also tend to argue for $T_\perp/T_\parallel < 1$ for the suprathermal electron component.

In Fig. 13, we show a scatter plot of ion temperature vs. proton densities (red) and water group ion densities (blue). The purpose of this plot is to see if there is any polytropic relationship for the two ion populations. For example, as the gas expands, both the density and temperature should decrease together. Overall, we see just the opposite, which indicates that the dominant source of ion energy comes from the pickup process which tends to increase with increasing radial distance, while the density decreases with r. In the case of protons we see a change of slope at lower temperatures and higher densities. One can show that this decrease is caused by the spacecraft dipping deeper into the plasma sheet near the ring plane where the proton densities are lower. That is, the field-aligned ambipolar electric field tends to float the protons above the ring plane. The black data points correspond to the pickup energy (derived from the local ion bulk speed) divided by the ratios $R_H \sim 3.2$ for protons (red) and $R_W \sim 4.0$ for water group ions (blue), respectively. This result is consistent with the sonic Mach number of ~ 2 for both species, with protons being more isotropic. The data is consistent with ambient ions being produced by the pickup process and then cooled after pickup. This could be done by outward radial transport combined with adiabatic cooling. Other possibilities are collisions between ambient ions and thermal electrons,
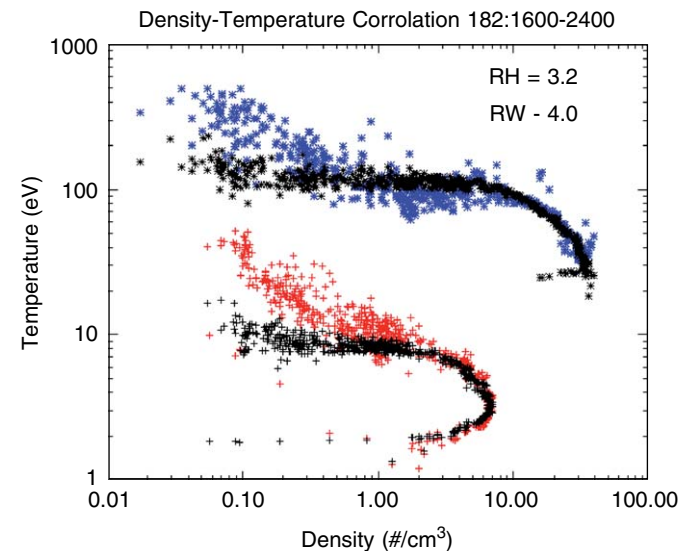

Fig. 13. Scatter plot of proton temperature vs. proton density (red) and water group ion temperature vs. water group ion density (blue). The black curves correspond to the pickup energy, $1/2\,M\,V_\phi^2$, divided by factor $R_H = 3.2$ for protons and $R_W = 4.0$ for water group ions. We used the azimuthal velocities for water group ions for both protons and water group ions.

radiation of energy induced by collisions or ion-neutral collisions. Further out, where the temperatures are higher, the data is more consistent with local pickup (i.e., reside above the black crosses) and very little cooling since they have energies closer to their pickup energy.

In Fig. 14, we show a plot of the total ion density, protons plus water group ions, vs. dipole L. The figure has curves superimposed on the data with power law dependences where the indices $n = 4$ (green), 6 (red) and 8 (blue) for $L > 6$. If total flux tube content were preserved with increasing dipole L, we would expect an index ~ 4 (green line), but the data is more consistent with an index ~ 6 (red line). This result could be caused by the spacecraft moving above the plasma sheet as one moves radially away from Saturn. We could also be seeing an increase in ion pressure anisotropy, $T_\perp/T_\parallel$, as one moves to larger radial distances. This dependence is indicative of an internal source of plasma that resides inside Rhea's L shell. Finally, islands of plasma breaking off from the plasma sheet outer boundary due to a centrifugal instability effect (Sittler et al., 2006b) could result in an increase in the negative radial gradient of the plasma sheet density if the spacecraft was relatively close to this outer boundary.

In Fig. 15, we use a similar plot, but now for the ion temperature. We see a definite increase in T_H and T_W with increasing radial distance as mentioned earlier. The protons have an L dependence of $T_H \sim L^{2.5}$, which is steeper in L than the water group ion dependence, $T_W \sim L^2$. In both cases, the temperature shows the expected L^2 for ion pickup. The lower power law index for water group ions can be traced to an increase in temperature inside Enceladus' L shell. This could be caused by the presence of a new population confined very close to the equatorial plane with $T_\perp/T_\parallel >> 5$. These ions would represent freshly picked up ions that have not yet equilibrated with
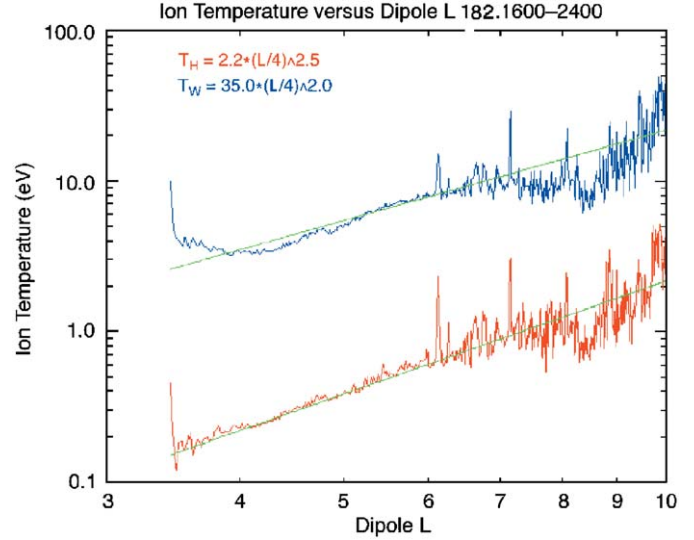
Fig. 15. Log–log plot of ion temperature vs. dipole L. We have super-imposed two manually derived power law fits. An L^2 dependence is consistent with local pickup since the azimuthal velocity $V_\phi = \Omega L \sin^3 \theta$ with $\Omega = $ angular velocity of Saturn. θ is the co-latitude of the observation site and the pickup energy per unit mass is $E_{PU}/M_H \propto V_\phi^2 \propto L^2$.

the ambient plasma. Furthermore, their latitudinal extent would be dictated by the scale height of the neutral clouds residing within Saturn's inner magnetosphere.

5.4. Closing remarks

We have presented improved estimates of the ion fluid parameters from the CAPS instrument for Saturn's inner plasmasphere. Preliminary results were presented by Sittler et al. (2005). They are qualitatively consistent to those estimated from Voyager plasma measurements. In addition we have determined the temperatures of protons and electrons within the inner magnetosphere which are lower than what Voyager could determine. We find that the plasma is dominated by water group ions and protons. The plasma is primarily close to corotation inside of Dione's L shell and further out starts to show evidence of sub-corotation. There is a definite anti-correlation between variations of V_R and V_ϕ which is consistent with conservation of angular momentum in the magnetosphere. This effect is also present in the Voyager data (Sittler et al., 2006b). The observations also show injection events of low density, hot plasma from the outer magnetosphere to the inner magnetosphere (Burch et al., 2005). These events show negative V_R. We have shown for the first time, definite observational evidence for outward transport with flux tube transfer events super-imposed upon the data. There is a definite positive radial gradient in the radial velocities and that it shows an L dependence for $D_{LL} \sim L^n$ with $n \sim 11$ (If purely diffusive transport, while in reality we have both diffusive and convective transport terms) for fixed stochastic time scale δt, while for centrifugal transport one normally uses $n \sim 3$. These results will impose a definite constraint on any future models of radial
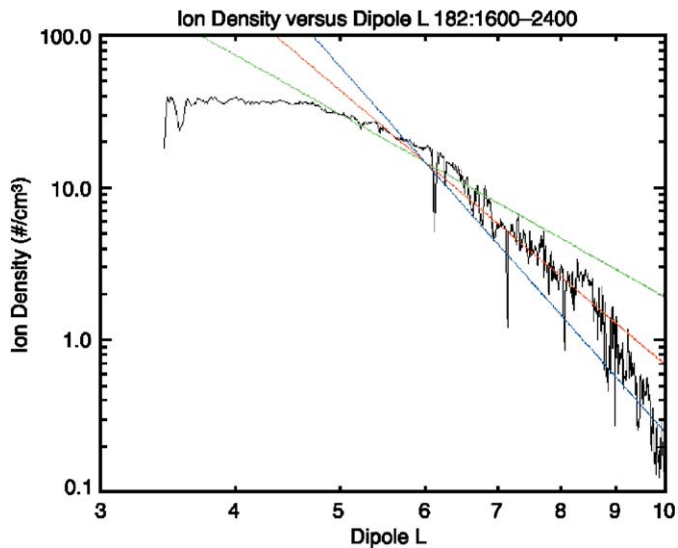

Fig. 14. Log–log plot of total ion density vs. dipole L. We have also super-imposed curves with power law dependences $1/L^\alpha$ with $\alpha = 4$ (green), 6 (red) and 8 (blue), respectively.

transport within Saturn's magnetosphere. The protons appear to be super-rotating within the inner magnetosphere, however this is due to a negative spacecraft potential. We confirm this interpretation by comparing ion and electron densities and using the thermal electron temperature. Outside of Rhea's L shell we derive a negative potential by enforcing the protons and water group ions to be co-moving, but the ELS data show photo-electrons, indicating that the spacecraft is positively charged. Therefore, there may be a slight systematic error leading to protons moving faster than the water group ions. Since the water group ions have energies $E/Q >> \Phi_{SC}$, they provide the best estimates of the ion flow velocity.

Based on the thermal properties of the ions and electrons, pickup seems to be the dominant source of energy to the plasma. The correlations between proton and water group ion temperatures suggest that dissociation of water molecules and ions is the primary source of proton heating. Pickup is also consistent with the proton and thermal electron temperatures being positively correlated. As discussed by Barbosa (1986, 1987), an ion beam instability resulting from the pickup process heats the electrons via lower hybrid waves. Such a process would need to be confirmed by the plasma wave in situ measurements. We also found that the ion density variation with dipole L was steeper than expected for constant total flux tube content, which could be caused by the changing latitude and/or changing pitch angle distributions. Erosion of the plasma sheet outer boundary via interchange motion may be another mechanism for this effect. The ion temperature radial gradients $\sim L^2$ are consistent with ion pickup as the dominant source of energy for the plasma.

In conclusion, these results will to lead to further insights into understanding Saturn's magnetosphere and the spatial distribution and compositional makeup of neutrals injected into Saturn's magnetosphere. The comparison of these results with other measurements, such as magnetometer data is ongoing and expected to provide further understanding of Saturn's magnetosphere and planetary magnetospheres in general.

Acknowledgments

Appendix A

Ion moment algorithm

As discussed in Sittler et al. (2005), the ion moment algorithm was implemented by taking the first order velocity moment of each species, adjusting the flow velocity in a Saturn inertial frame (i.e., removed spacecraft velocity in Saturn frame), shifting the velocity of each data point into the proper frame, and then taking the mirror image of each data point in the proper frame (i.e., we assume gyrotropy). We then transform into the instruments collimator plane (see Young et al. (2004) for physical properties of instruments collimator and its FOV). In the collimator frame, we make sure double counting in velocity space does not occur. The data are then mapped out of the collimator plane of the instrument (i.e., we assume the ion distribution is isotropic) so that we can approximate the 4π coverage needed for our moment integrations. We know that the isotropy approximation is violated in a number of regions. We then transform back into the Saturn inertial frame after computing the flux or first-order moment. The 2D velocity space "frame" is that defined by the instrument collimator. The flow velocities are defined in terms of a Saturn-centered cylindrical coordinate system (V_R, V_ϕ, V_Z). The measurements are effectively 2D, but since the instruments FOV is tilted $\sim 38°$ from the equatorial plane (i.e., this tilt is such that the instruments collimator frame intersects Saturn's equatorial plane), the azimuthal velocity V_ϕ and cylindrical radial velocity V_R are more constrained, while V_Z is less constrained. This algorithm is implemented independently for H^+ and W^+. Once the proper frame flow velocity is known, we can compute the zeroth-order moment in the proper frame for the ion density N_i and take the second moment in the proper frame to compute the ion pressure P_i. Then by taking the ratio of P_i and N_i we can get an estimate of the ion temperature T_i (i.e., $T_i = P_i/(N_i k_B)$ with $P_i = 1/3(Tr\,P)$, where k_B is Boltzmann's constant). We also have the capability to shift each data point in energy space by the spacecraft potential Φ_{sc} along the radial direction relative to the center of the spacecraft (i.e., we assume the Debye Length λ_D of the plasma and photo-electrons is much larger than the dimensions of the spacecraft). This allows us to take into account the effect of spacecraft charging on the fluid calculations.

Derivation of ion moment algorithm

Our approach to performing the velocity moments of the ion coincidence counts as a function of energy-per-charge (E/Q_i) and angular sector ϕ_j, was to make a minimal number of assumptions about the ion velocity distribution functions $f(\vec{v}_{i,j})$. For example, we do not make assumptions by adopting convected bi-Maxwellian, shell or kappa distribution functions. Before reading this section, we request the reader refer to the Young et al. (2004) paper to become more familiar with the instrument characteristics, mounting with the spacecraft, and how data is acquired by the instrument. Since, for SOI the actuator angle was fixed we had to make an assumption of isotropy when mapping the data out of the collimator frame of the instrument. Within the collimator frame, we translated to the ion

proper frame and then added the mirror image of the data to fill the velocity space so that we could perform our integrations. In doing this we made sure we did not double count contributions to the velocity integrations. We use the fact that $f(\vec{v}_{i,j})$ and d^3v are invariants during a linear translation or rotation in velocity space (Rossi and Olbert, 1970). This concept turns out to be a very powerful tool for computing our velocity moments whenever the instrument does not cover all 4π space. Use of the coincidence ion data has the important feature of separating protons and water group ions in E/Q_i space and works reliably in velocity space for each of the two species. An exception to this rule is the contamination of the proton TOF channels by water group ions due to ion scattering within the IMS. The algorithm works well when the flow velocity of the ions is confined near the instrument's collimator plane and directed into one of the eight angular sectors of the instrument. Experience has shown that when the cold ion beam does not meet these requirements, one cannot reconstruct the ion distribution function and compute the velocity moments. But, it may be possible to extract information about the hot ion component which is more isotropic and can be viewed during poor viewing periods. During the end of our analysis period at ~182:2400 SCET when the spacecraft performs a roll maneuver and we no longer see the cold beam, the remaining hot component is found to be corotating. This was done by constraining the flow from deviating too much from corotation. Under these circumstances we were able to extract information about the hot component such as density and temperature.

Compute distribution function

As discussed in Young et al. (2004), the standard formula for computing the ion distribution function is given by

$$f_k(\vec{v}_{i,j}) = CR(k,i,j)M_k^2/(2E_i^2 G_k \Delta t) \qquad (A.1)$$

with G_k being the differential geometric factor of the IMS

$$G_k = A\varepsilon_k\tau_k\langle\Delta\Omega\Delta E/E\rangle, \qquad (A.2)$$

where $CR(k,i,j)$ is the count rate for ion k at energy step i and angular sector j, while A is the instrument's entrance aperture area, $\varepsilon_k(E_i, M_k)$ is the energy and mass dependent efficiencies of the instrument carbon foils, detectors, and electronics, $\tau_k(E_i, M_i)$ is the energy and mass dependent transmission of the instrument foils, grids and optics and $\langle\Delta\Omega\Delta E/E\rangle$ is the solid angle and fractional energy pass band of the IMS. In the case of the water group ions we performed a weighted sum of the geometric factors for each sub-species (i.e., O^+, OH^+, H_2O^+, H_3O^+) based on their relative abundances in the TOF spectra at the 15 min resolution level (Fig. 2 in Sittler et al. (2005) is an example of the TOF data summed over a 6 h interval):

$$G_W = \sum_{k=1}^{4} W_k G_k \quad \text{with} \quad \sum_{k=1}^{4} W_k = 1. \qquad (A.3)$$

The same can be said for the mean water group ion mass

$$M_W = \sum_{k=1}^{4} W_k M_k. \qquad (A.4)$$

We are now in a position to apply our ion moments algorithm.

Determine ion flow velocity

We first rotate the velocity vectors for each observational site from the sensor frame to the actuator frame, $\vec{v}_{A,i,j} = \overset{\leftrightarrow}{\underset{S,A}{R}} \vec{v}_{S,i,j}$, from the actuator frame to the spacecraft frame, $\vec{v}_{SC,i,j} = \overset{\leftrightarrow}{\underset{A,SC}{R}} \vec{v}_{A,i,j}$, and from the spacecraft frame to the Saturn inertial orbital (SIO) frame, $\vec{v}_{SAT,i,j} = \overset{\leftrightarrow}{\underset{SC,SAT}{R}} \vec{v}_{SC,i,j}$. We then remove the spacecraft motion from the observation sites, since $\vec{V}_{SC}$, is given in SIO, $\vec{v}'_{SAT,i,j} = \vec{v}_{SAT,i,j} + \vec{V}_{SC}$. We are now in a position to translate the observation sites into the plasma proper frame in SIO coordinates. Since we have an iterative algorithm, we first assume that the ion flow velocity is equal to the corotation velocity $\vec{V} = \vec{V}_{COR}$. We then shift all our observation sites into the assumed proper frame; i.e., $\vec{v}'_{SAT,i,j} \rightarrow \vec{w}_{i,j} = \vec{v}'_{SAT,i,j} - \vec{V}$. At this point we make use of the rule that the distribution function $f(\vec{v}_{i,j})$ and velocity volume element d^3v are invariant for a linear velocity translation or a rotation, so that $f(\vec{v}_{i,j}) \rightarrow f(\vec{w}_{i,j})$ and we can use the same $d^3v = v_{i,j}^2\,dv_i\,d\Omega_j$ in going from the sensor frame to the proper frame $\vec{w}_{i,j}$. But, before we can proceed, we must first rotate our observation sites into the sensor collimator frame. We need to do this so we can fill up the 4π space above and below the collimator frame. To determine the collimator frame, while in the ion proper frame we perform the cross product $\hat{n}_{COLL} = \vec{w}_{i,j} \times \vec{w}_{i,j+1}$ which defines the normal to the collimator frame. We do this for all j ($1\leqslant j\leqslant 8$) and compute the mean. This cross product is computed at the highest energies ~50 kV to ensure we are in the collimator frame. Once this is done, we can compute the rotation matrix that allows use to rotate $\vec{w}_{i,j}$ into the collimator frame $\vec{w}_{COLL,i,j} = \overset{\leftrightarrow}{\underset{SAT,COLL}{R}} \vec{w}_{i,j}$.

Since, the CAPS IMS only samples data for $160°$ in the collimator frame, we take the mirror image of the data points, which are now represented in the proper frame, to fill up the $360°$ space with an angular resolution ~$20°$ (i.e., $\vec{w}_{COLL,i,j} \rightarrow -\vec{w}_{COLL,i,j}$). We would not be able to do this if we were not in the proper frame. As before, we take advantage of the invariance $f(\vec{v}_{i,j})$ and $d^3v = v_{i,j}^2\,dv_i\,d\Omega_j$ when we take the mirror image. But, before we proceed any further, we must first eliminate "double counting". We do this by excluding all mirror image points that do not satisfy the inequality $(\vec{v}_{A,i,j} > 2\vec{V}) \bullet \hat{e}_y$ where the y-axis points radially away from the rotation axis of the actuator. This relationship is applied to the observation sites in the actuator frame moving with the spacecraft to ensure that

the mirror points only occupy the region not sampled by the instrument in the collimator frame. We are now in a position to fill up the velocity space out of the collimator frame. To do this we assume that the distribution function is isotropic in the proper frame. We then elevate in θ our observations, for each angular sector ϕ_j with $\theta_{j,m=0} \sim \pi/2$, for the range $5° \leqslant \theta_{j,m} \leqslant \pi - 5°$ at a step size $\Delta\theta \sim 10°$. Then, for each new data point, we take the mirror image to completely fill up the 4π steradian space. Since, the sensor $\Delta\Omega = \sin\theta\, d\theta\, d\phi$ is defined at $\theta \sim \pi/2$, we must multiply each observation site by $\sin\theta$ to correctly estimate the volume element in velocity properly. Otherwise, we will "over-sample" the data in velocity space and over-estimate various parameters; e.g., the ion density, as shown below.

Now that the velocity space is completely filled, with corresponding $f(\vec{v}_{i,j})$ and $d^3v = v_{i,j}^2\, dv_i\, d\Omega_j$ at each lattice site, we can proceed with our estimation of the ion flux or first-order moment

$$\vec{F} = \sum_{i,j,m} f(\vec{w}_{COLL,i,j,m})\vec{w}_{COLL,i,j,m} v_{i,j}^2\, dv_i\, \sin\theta_m\, d\theta_m\, d\phi_j$$

$$(A.5)$$

followed by rotating the flux $\vec{F}$ into the Saturn inertial orbital frame. We then test to see if the flux $\vec{F}$ has changed sign. If not we increment the flow velocity $\vec{V}$ by $\delta\vec{V}$ (i.e., $\vec{V} \to \vec{V} + \delta\vec{V}$ if $\vec{F} > 0$ or $\vec{V} \to \vec{V} - \delta\vec{V}$ if $\vec{F} < 0$). We then repeat all the steps noted above where we translate the observation sites into the new proper frame and compute the flux $\vec{F}$ again. We do this for each velocity component separately until a flip in sign occurs for each of the components. We then change the step size $\delta\vec{V} \to \delta\vec{V}/2$, recompute $\vec{V} \to \vec{V} + \delta\vec{V}$ if $\vec{F} > 0$ or $\vec{V} \to \vec{V} - \delta\vec{V}$ if $\vec{F} < 0$, repeating all the steps as before to get a new estimate of the flux $\vec{F}$ until $\delta\vec{V} < \eta\vec{V}_{COR}$ where $\eta \sim 1\%$. When this happens, $\vec{F} \to 0$ and get the true proper frame velocity of the ion flow is obtained. We do this separately for H^+ and W^+.

Compute density and pressure moments

Once the ion flow velocity is known, it is straight forward to compute the ion density and ion pressure. The ion density is given by the expression

$$n_k = \sum_{i,j,m} f_k(\vec{w}_{COLL,i,j,m}) v_{i,j}^2\, dv_i\, \sin\theta_m\, d\theta_m\, d\phi_j \quad (A.6)$$

the ion pressure by

$$P_k =$$
$$1/3 M_k \sum_{i,j,m} f_k(\vec{w}_{COLL,i,j,m}) w_{COLL,i,j,m}^2 v_{i,j}^2\, dv_i\, \sin\theta_m\, d\theta_m\, d\phi_j$$

$$(A.7)$$

and $k = H^+$ or W^+. We can then solve for the ion temperature using the relationship

$$T_k = P_k/(n_k k). \quad (A.8)$$

Corrections due to temperature anisotropy and $\sin\theta$ term

Assuming a bi-Maxwellian distribution function in the ion proper frame

$$f_{BM}(\vec{w}) = \frac{n}{\pi^{3/2} w_{c||} w_{c\perp}^2}\, e^{-(w_{||}^2/w_{c||}^2 + w_\perp^2/w_{c\perp}^2)}. \quad (A.9)$$

We can write the density integral as follows:
$n = \int\int\int f_{BM}(\vec{w}) w_\perp\, dw_\perp\, dw_{||}\, d\phi$, then if we set $w_{c||}^2 = w_\perp^2$ in the exponential term for isotropy the integral has the form

$$n = \frac{2n_0}{\sqrt{\pi} w_{c||} w_{c\perp}^2} \int \exp(-w_\perp^2/w_{c\perp}^2) w_\perp\, dw_\perp$$

$$\times \int \exp(-w_{||}^2/w_{c\perp}^2)\, dw_{||}$$

$$= \frac{2n_0}{w_{c\perp}^2}\left(\frac{w_{c\perp}}{w_{c||}}\right) \int \exp(-w^2/w_{c\perp}^2) w\, dw, \quad (A.10)$$

which then reduces to $n = n_0\sqrt{T_\perp/T_{||}}$

The correction for the pressure is given by

$$P_k = \frac{n_0 M_k}{3\pi^{3/2} w_{c||} w_{c\perp}^2} \int \exp(-w_\perp^2/w_{c\perp}^2 - w_z^2/w_{||}^2)$$

$$\times (w_{||}^2 + w_\perp^2) w_\perp\, dw_\perp\, dw_{||}\, d\phi = \sqrt{\frac{T_\perp}{T_{||}}}\frac{1}{2} n_0 M_k w_{c\perp}^2$$

$$(A.11)$$

for which we have set $w_{c|||}^2 = w_{c\perp}^2$. Dividing by Eq. (A.11) by (A10) one gets $T_k = 1/2 M_k w_{c\perp}^2$.

We estimate the error by ignoring the $\sin\theta$ term. Using spherical coordinates for an isotropic Maxwellian we get

$$n = \frac{n_0}{\pi^{3/2} w_c^3} \int\int\int \exp(-w^2/w_c^2) w^2\, dw\, d\theta\, d\phi$$

$$= \frac{n_0 2\pi^2}{\pi^{3/2}} \int \exp(-x^2) x^2\, dx = n_0 \frac{\pi}{2}. \quad (A.12)$$

We estimate the correction for the pressure P_k ignoring the $\sin\theta$ term.

$$P_k = \frac{n_0 M_k}{3\pi^{3/2} w_c^3} \int\int\int \exp(-w^2/w_c^2) w^4\, dw\, d\theta\, d\phi$$

$$= \frac{n_0 M_k 2\pi^2 w_c^2}{3\pi^{3/2}} \int_0^\infty \exp(-x^2) x^4\, dx = \frac{\pi}{2} P_{k0}, \quad (A.13)$$

where P_{k0} is the pressure we would get with $\sin\theta$ term included. When we divide (A.13) by (A.12), we get $T_k = 1/2 M_k w_{c\perp}^2$, which is the same when we include the $\sin\theta$ term (i.e., no correction as concluded from Figs. 3 and 4).

Appendix B

Correction for Fig. 3 in Sittler et al. (2005)

In Fig. 3 of Sittler et al. (2005), they have plotted the Sonic Mach numbers for H^+ and W^+ ions, Alfvèn Mach number and plasma beta vs. SCET time. Unfortunately, there was a plotting error for the Alfvèn Mach number.
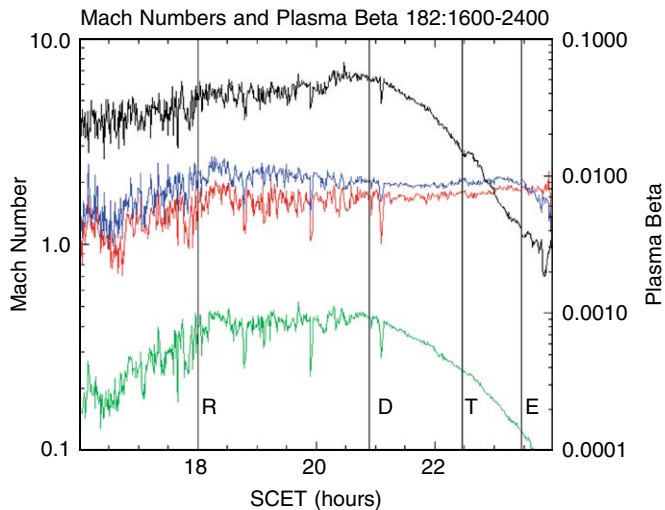
Mach Numbers and Plasma Beta 182:1600-2400

Fig. B1. The Alfvèn Mach number (green), Sonic Mach number for protons (red) and water group ions (blue) and plasma beta (black) vs. time derived from data in Figs. 3 and 4. Uncertainties are at most ∼10% for the Mach numbers and ∼20% in an absolute sense for the plasma beta. The Alfvèn Mach numbers reported here supersede that presented in Sittler et al. (2005) Fig. 3 due to a plotting error in that paper.

Here, in Fig. B1 we have a corrected plot that extends the time coverage from 1800–2400 to 1600–2400 h on day 182 (30 June 2004). In the revised plot, the Alfvèn Mach number turns over to lower values beyond the orbital position of Rhea.

References

Andrè, N., et al., 2006. Plasma transport signatures at Saturn observed during Cassini inbound orbit insertion. European Geosciences Union, EGU06-A-07580.

Barbosa, D.D., 1986. Medium energy electrons and heavy ions in Jupiter's magnetosphere: effects of lower hybrid wave-particle interactions. J. Geophys. Res. 91, 5605–5615.

Barbosa, D.D., 1987. Titan's atomic nitrogen torus: inferred properties and consequences for the Saturnian aurora. Icarus 72, 53.

Bridge, H.S., et al., 1981. Plasma observations near Saturn: initial results from Voyager 1. Science 212, 217.

Bridge, H.S., et al., 1982. Plasma observations near Saturn: initial results from Voyager 2. Science 215, 563.

Burch, J.L., Goldstein, J., Hill, T.W., Young, D.T., Crary, F.J., Coates, A.J., Andre, N., Kurth, W.S., Sittler Jr., E.C., 2005. Properties of local plasma injections in Saturn's magnetosphere. Geophys. Res. Lett. 32 (14), L14S02.

Cowley, S.W.H., Badman, S.V., Bunce, E.J., Clarke, J.T., Gerard, J.-C., Grodent, D., Jackman, C.M., Milan, S.E., Yeoman, T.K., 2005. Reconnection in a rotation-dominated magnetosphere and its relation to Saturn's auroral dynamics. J. Geophys. Res. 110, A02201.

Frank, L.A., Burek, B.G., Ackerson, K.L., Wolfe, J.H., Mihalov, J.D., 1980. Plasmas in Saturn's magnetosphere. J. Geophys. Res. 85, 5695.

Hill, T.W., Rymer, A.M., Burch, J.L., Crary, F.J., Young, D.T., Thomsen, M.F., Delapp, D., Andrè, N., Coates, A.J., Lewis, G.R., 2005. Evidence for rotationally driven plasma transport in Saturn's magnetosphere. Geophys. Res. Lett. 32, L14S10.

Johnson, R.E., Liu, M., Sittler Jr., E.C., 2005b. Plasma-induced clearing and redistribution of material embedded in planetary magnetospheres. Geophys. Res. Lett. 32, L24201.

Jurac, S., Johnson, R.E., Baragiola, R.A., Sittler, E.C., 1995. Charging of ice grains by low-energy plasma: application to Saturn's E ring. J. Geophys. Res. 100, 14,821–14,831.

Krimigis, S.M., et al., 2005. Dynamics of Saturn's magnetosphere from MIMI during Cassini's orbital insertion. Science 307, 1270.

Lazarus, A.J., McNutt Jr., R.L., 1983. Low-energy plasma ion observations in Saturn's magnetosphere. J. Geophys. Res. 88, 8831.

Mauk, B.H., et al., 2005. Geophys. Res. Lett 32, L14S05.

McComas, D.J., Nordholt, J.E., Bame, S.J., Barraclough, B.L., Gosling, J.T., 1990. Linear electric field mass analysis: a technique for three-dimensional high mass resolution space plasma composition measurements. Proc. Nat. Aca. Sci. USA 87, 5925.

McComas, D.J., Nordholt, J.E., 1990. A new approach to 3-D, high sensitivity, high mass resolution space plasma composition measurements. Rev. Sci. Instrum. 61, 3095.

McComas, D.J., Nordholt, J.E., Berthelier, J.-J., Illiano, J.-M., Young, D.T., 1998. The Cassini ion mass spectrometer, measurement techniques in space plasmas: particles. In: Pfaff, R.F., Borovsky, J.E., Young, D.T. (Eds.), Geophysical Monograh 102, pp. 187.

Moncuquet, M., Lecacheux, A., Meyer-Vernet, N., Cecconi, B., Kurth, W.S., 2005. Quasi-thermal noise spectroscopy in the inner magnetosphere of Saturn with Cassini/RPWS: electron temperatures and density. Geophys. Res. Lett. 32, L20S02.

Nordholt, J.E., Berthelier, J.J., Burr, D., Funsten, H.O., Goldstein, R., Illiano, J.M., McCabe, K.P., McComas, D.J., Potter, D.M., Young, D.T., 1998. The Cassini ion mass spectrometer: performance measures and techniques, measurement techniques in space plasmas: particles. In: Pfaff, R.F., Borovsky, J.E., Young, D.T., Geophysical Monograph 102, pp. 209.

Richardson, J.D., 1986. Thermal ions at Saturn: plasma parameters and implications. J. Geophys. Res. 91, 1381.

Richardson, J.D., Sittler Jr., E.C., 1990. A plasma density model for Saturn based on Voyager observations. J. Geophys. Res. 95, 12019.

Richardson, J.D., Eviatar, A., McGrath, M.A., Vasyliunas, V.M., 1998. OH in Saturn's magnetosphere: observations and implications. J. Geophys. Res. 103, 20245.

Rossi, B., Olbert, S., 1970. Introduction to the Physics of Space. McGraw-Hill.

Rymer, A.M., 2004. Analysis of Cassini plasma and magnetic field measurements from 1-7 AU, Ph.D. Thesis, UCL.

Schultz, M., Lanzerotti, L.J., 1974. Particle Diffusion in the Radiation Belts. Springer, Berlin.

Siscoe, G.L., Summers, D., 1981. Centrifugally driven diffusion of Iogenic plasma. J. Geophys. Res. 86, 8471.

Sittler Jr., E.C., Ogilvie, K.W., Scudder, J.D., 1983. Survey of low-energy plasma electrons in Saturn's magnetosphere: Voyagers 1 and 2. J. Geophys. Res. 88, 8847.

Sittler Jr., E.C., 1993. Real-time spectral analysis algorithm for space plasma three-dimension ion mass spectrometers. Rev. Sci. Instr. 64, 2771.

Sittler Jr., E.C., Thomsen, M., Chornay, D., Shappirio, M.D., Simpson, D., Johnson, R.E., Smith, H.T., Coates, A.J., Rymer, A.M., Crary, F., McComas, D.J., Young, D.T., Reisenfeld, D., Dougherty, M., Andre, N., 2005. Preliminary results on Saturn's inner plasmasphere as observed by Cassini: comparison with Voyager. Geophys. Res. Lett. 32, L14S07.

Sittler Jr., E.C., et al., 2006a. Energetic nitrogen ions within the inner magnetosphere of Saturn. J. Geophys. Res., in press.

Sittler Jr., E.C., Blanc, M.F., Richardson, J.D., 2006b. Proposed model of Saturn's auroral response to the solar wind: centrifugal instability model. J. Geophys. Res. 111, A06208.

Wolfe, J.H., Mihalov, J.D., Collard, H.R., McKibbin, D.D., Frank, L.A., Intriligator, D.S., 1980. Preliminary results on the plasma environment of Saturn from the pioneer 11 plasma analyzer experiment. Science 207, 403.

Young, et al., 2004. Cassini plasma spectrometer investigation. Space Sci. Rev. 114, 1–112.

Young, et al., 2005. Composition and dynamics of plasma in Saturn's magnetosphere. Science 307, 1262.